ATLAS NOTE

ATLAS-CONF-2014-005

March 4, 2014

A search for resonant Higgs-pair production in the $b\bar{b}b\bar{b}$ final state in pp collisions at $\sqrt{s} = 8\,\mathrm{TeV}$

The ATLAS Collaboration

Abstract

A search for TeV-scale resonances decaying via a pair of Higgs bosons to the $b\bar{b}b\bar{b}$ final state is performed using $19.5\,\mathrm{fb}^{-1}$ of proton-proton collision data at $\sqrt{s} = 8\,\mathrm{TeV}$ recorded by ATLAS in 2012. The search assumes a Standard Model Higgs boson with a mass of $125\,\mathrm{GeV}$. The decay of each Higgs boson is reconstructed from a pair of b-tagged jets that have small angular separation and form a dijet system with transverse momentum greater than $200\,\mathrm{GeV}$. The bulk Randall-Sundrum model with a warped extra dimension and a coupling of $k/\bar{M}_{\mathrm{Pl}} = 1.0$ is used as a benchmark to search for resonances, corresponding to the first Kaluza-Klein excitation mode of the graviton G^*, in the range between $500\,\mathrm{GeV}$ and $1500\,\mathrm{GeV}$. No evidence of a signal is found, and upper limits on $\sigma(pp \to G^*) \times \mathrm{BR}(G^* \to HH \to b\bar{b}b\bar{b})$ are derived, giving an observed limit of 7 fb at the 95% confidence level for a KK graviton mass of 1 TeV. The benchmark model is excluded at the 95% confidence level for KK graviton masses between $590\,\mathrm{GeV}$ and $710\,\mathrm{GeV}$.

1   Introduction

The decays of TeV-scale resonances to pairs of electroweak-scale bosons are predicted in many new physics models [1–6], and have already been searched for in various $WW/ZZ/WZ$ topologies at the LHC [7–14]. The Higgs boson discovery [15, 16] has opened up further opportunities for searches, in particular for resonant pair production of a Standard Model (SM) Higgs H, predicted in several of these models [4–6]. A search for resonant di-Higgs production in the context of "Two Higgs Doublet Model" (2HDM) extensions of the Higgs sector [6] has recently been carried out by CMS [17], for resonance masses up to 360 GeV, using multilepton final states with and without diphoton candidates. A recent particle level study [18] indicated that the $X \rightarrow HH \rightarrow b\bar{b}b\bar{b}$ final state is promising for higher-mass resonance searches, benefitting from the large expected branching ratio of Higgs decays to b-quark pairs and the high transverse momentum (p_{T}) with which the b-quarks are produced.

This document describes a search for TeV-scale resonances decaying to a pair of SM Higgs bosons, both of which subsequently decay to $b\bar{b}$, leading to two back-to-back, high p_{T}, doubly b-tagged dijet systems. The individual Higgs decays are reconstructed from pairs of nearby $R = 0.4$ anti-k_{t} jets [19], each b-tagged with a multivariate b-tagging algorithm [20]. The invariant masses of the dijets are required to be consistent with the $H \rightarrow b\bar{b}$ hypothesis, assuming $m_H = 125$ GeV, and the invariant mass of the four b-tagged jets that make up the two dijet systems, $m_{4\mathrm{j}}$, is examined to look for a resonance.

The search is performed with a data sample corresponding to $19.5\,\mathrm{fb}^{-1}$ of proton-proton collisions recorded by the ATLAS detector in 2012 at $\sqrt{s} = 8$ TeV. The results are interpreted using as a signal the first Kaluza-Klein (KK) excitation of the graviton (G^*) in a Randall-Sundrum (RS) model [3] with a warped extra dimension, in the context of the "bulk RS model" in which the fermion and boson fields of the SM are free to propagate into the extra dimension [4, 21]. This is the baseline signal model used in a number of searches for resonant electroweak-scale boson production [7–10]. As well as decaying to $t\bar{t}$, W^+W^- and ZZ, the G^* also decays to a pair of Higgs bosons with a reasonably large branching fraction of ~7%. Within this model, the dimensionless coupling constant $k/\bar{M}_{\mathrm{Pl}}$, where k is the curvature of the warped extra dimension and $\bar{M}_{\mathrm{Pl}} = M_{Pl}/\sqrt{8\pi}$ is the reduced Planck mass, is set to unity. The G^* production cross-section and decay width are proportional to the square of the coupling, and with $k/\bar{M}_{\mathrm{Pl}} = 1.0$ the natural width of the G^* resonance is smaller than the $m_{4\mathrm{j}}$ resolution (~15%). For a KK Graviton mass (m_{G^*}) of 500 GeV, the BR($G^* \rightarrow HH$) is 6.4%, the G^* width is 19 GeV, and the production cross-section $\sigma(pp \rightarrow G^*) \times$ BR($G^* \rightarrow HH \rightarrow b\bar{b}b\bar{b}$) is 71 fb. For $m_{G^*} = 1$ TeV, the BR($G^* \rightarrow HH$) is 7.4%, the width is 56 GeV, and $\sigma(pp \rightarrow G^*) \times$ BR($G^* \rightarrow HH \rightarrow b\bar{b}b\bar{b}$) is 1.5 fb.

As part of this study, a search for $G^* \rightarrow ZZ \rightarrow b\bar{b}b\bar{b}$ was also performed using the same analysis strategy but with a modified signal region definition. However, the sensitivity was found to be significantly lower than that demonstrated in the $ZZ \rightarrow llq\bar{q}$ final state [7, 8], and the results are not reported here.

2   The ATLAS Detector

The ATLAS detector [22] is a general-purpose detector with an inner tracking system, calorimeters and an outer muon spectrometer. The tracking system consists of silicon pixel, silicon microstrip and transition-radiation straw-tube detectors. This system is immersed in a 2 T axial magnetic field produced by a solenoid and provides charged-particle tracking and identification in the pseudorapidity[1] region $|\eta| < 2.5$. The central calorimeter system in the pseudorapidity range $|\eta| < 1.7$ consists of a liquid-argon electromagnetic sampling calorimeter with high granularity and an iron/scintillator tile calorimeter

---

[1]ATLAS uses a right-handed coordinate system with its origin at the nominal interaction point (IP) in the centre of the detector and the z-axis along the beam pipe. The x-axis points from the IP to the centre of the LHC ring, and the y-axis points upwards. Cylindrical coordinates (r, ϕ) are used in the transverse plane, ϕ is the azimuthal angle around the beam pipe. The pseudorapidity, η, is defined in terms of the polar angle θ as $\eta = -\ln[\tan(\theta/2)]$.

providing hadronic energy measurements. The endcap and forward regions are instrumented with liquid-argon calorimeters for both electromagnetic and hadronic energy measurements up to $|\eta| = 4.9$. The muon spectrometer is operated in a toroidal magnetic field provided by air-core superconducting magnets and includes tracking chambers for precise muon momentum measurements up to $|\eta| = 2.7$ and trigger chambers covering the range $|\eta| < 2.4$.

3   Data and Simulated Samples

The data sample used in this analysis, after applying data quality requirements, corresponds to an integrated luminosity of $\mathcal{L} = 19.5 \pm 0.5\,\text{fb}^{-1}$. The uncertainty on the integrated luminosity (2.8%) is derived following the same methodology as that detailed in Ref. [23], from a calibration of the luminosity scale using beam-separation scans performed in November 2012.

Simulated Monte Carlo (MC) event samples are used to model the signal, as well as the small background contributions from top-pair production ($t\bar{t}$) and Z+jets events. The $G^* \to HH \to b\bar{b}b\bar{b}$ signal MC samples are generated with MADGRAPH v1.5.1 [24], interfaced to PYTHIA v8.175 [25] for parton showering (PS), hadronization and underlying-event (UE) simulation. The Higgs mass is fixed to 125 GeV, the BR($H \to b\bar{b}$) is set[2] to 57.7% [26], and the CTEQ6L1 leading-order (LO) parton-density function (PDF) [27] is used. Eleven samples are generated to cover a range of G^* masses from 500 GeV to 1500 GeV, at 100 GeV intervals. The $t\bar{t}$ background sample is generated using POWHEG v1.0 [28, 29] interfaced to PYTHIA v6.426, with the top mass fixed to 172.5 GeV, and the CT10 [30] next-to-leading order (NLO) PDF set. The NNLO+NNLL prediction of 253 pb for the $t\bar{t}$ cross-section [31–36] is used for normalisation. The Z+jets sample is generated using PYTHIA v8.165 with the CTEQ6L1 PDF, and the Z decaying to two b-quarks. The Z+jets cross-section is taken from a NLO POWHEG v1.0 plus PYTHIA v8.165 prediction, which is a factor 1.62 higher than the value given by PYTHIA alone.

The generated MC events are processed with the GEANT4-based [37] ATLAS detector simulation [38]. In the case of the $G^* \to HH \to b\bar{b}b\bar{b}$ signal samples, a fast version of the ATLAS detector simulation is used [39], which uses a parametrization of the calorimeter response [40], and GEANT4-based simulation for the remaining detector components. Use of the fast simulation was validated against a limited number of $G^* \to HH \to b\bar{b}b\bar{b}$ signal samples produced using the full GEANT4-based simulation. Effects of multiple proton-proton interactions in the same bunch crossing (pile-up) are included, and the MC simulated samples are re-weighted in such a way that the distribution of the average number of interactions per bunch crossing matches that in the data. The same reconstruction software is used to process both the data and the simulated samples.

4   Event Reconstruction

Jets are reconstructed from topological clusters of calorimeter cells [41] using the anti-k_t jet clustering algorithm [19], with radius parameter $R = 0.4$. The effects of pile-up on jet energies are accounted for by a jet-area-based correction [42]. Jets are then calibrated using p_T- and η-dependent calibration factors based on MC simulations and the combination of several *in situ* techniques applied to data [41]. If a muon that passes tight muon identification quality criteria [43] is within a cone of $\Delta R = \sqrt{\Delta \eta^2 + \Delta \phi^2} = 0.4$ from the jet axis, the four-momentum of the muon is added to that of the jet (after correcting for the energy already deposited by the muon in the calorimeter). To remove jets with significant contribution from pile-up interactions [44], jets with $p_\text{T} < 50$ GeV are required to have at least 50% of the p_T sum of

---

[2]MADGRAPH does not take into account decays of the Higgs to off-shell particles, such as WW^* or ZZ^*, and so gives an erroneously large $H \to b\bar{b}$ branching ratio that has been corrected.

tracks matched to the jet belonging to tracks originating from the primary vertex[3]. The entire event is vetoed if any jet with $p_T > 20$ GeV is identified as arising from non-collision backgrounds [45], such as calorimeter noise or beam-gas/halo events. This requirement removes less than 1% of the events in the data and signal MC samples.

Jets with $|\eta| < 2.5$ originating from b-quarks are identified ("b-tagged") by exploiting the properties of the tracks inside them, the most important being the impact parameter (defined as the track's distance of closest approach to the primary vertex in the transverse plane) of each track, the presence of a displaced vertex, and the reconstruction of charm and beauty hadron decays. The "MV1" b-tagging algorithm [20] used in this analysis combines the above information using a neural network and is configured to achieve an efficiency of 70% for tagging b-jets[4] in a MC sample of $t\bar{t}$ events.

5   Event Selection

The events of interest in this analysis were triggered [46] by a combination of five jet-based triggers that were not prescaled during data taking in 2012. The triggers are complementary and result in a very high trigger efficiency (> 99.5%) for $G^* \to HH \to b\bar{b}b\bar{b}$ MC events passing the full offline selection across the full G^* mass range considered. The trigger acceptance at all G^* masses is dominated by three triggers that each require the presence of one or more jets identified as b-jets by a dedicated high-level-trigger b-tagging algorithm, in combination with other requirements. At higher G^* masses these triggers are complemented by two triggers with high jet transverse energy (E_T) thresholds, but no b-tagging requirement. More details on the triggers used are given in Appendix A.

The event selection starts from the requirement of at least four b-tagged jets, each with $p_T > 40$ GeV. It is then required that two unique dijets (i.e., the two dijets do not have any jet in common) can be formed from the four highest-p_T b-tagged jets, where for each dijet system the angular distance, ΔR, between the jets is smaller than 1.5 and the transverse momentum of the system, p_T^{dijet}, is greater than 200 GeV. In the rare case that a jet can be used to create more than one dijet which satisfies the above kinematic requirements, the dijet with the highest mass is chosen. In order to reduce the $t\bar{t}$ background, a specific set of requirements is applied to the dijets in the event, referred to collectively as the "$t\bar{t}$ veto". Since top quarks mainly decay to three jets, "extra jets" in the event (jets not already used in the formation of the two dijets) are used to attempt to reconstruct the mass of the W and the mass of the top when combined with the dijet. These extra jets are required to have $p_T > 30$ GeV, $|\eta| < 2.5$, and $\Delta R < 1.2$ relative to the dijet. The mass of the W candidate, m_W, is reconstructed by taking the invariant mass of the system formed by the extra jet and the jet in the dijet system that has the lowest probability of being a b-jet according to the MV1 b-tagger. The mass of the top candidate, m_t, is reconstructed by taking the invariant mass of the system formed by the dijet and the extra jet. The compatibility with the top quark decay hypothesis is determined using the variable:

$$X_{tt} = \sqrt{\left(\frac{m_W - \tilde{m}_W}{\sigma_{m_W}}\right)^2 + \left(\frac{m_t - \tilde{m}_t}{\sigma_{m_t}}\right)^2},$$

where $\sigma_{m_W} = 0.1 m_W$, $\sigma_{m_t} = 0.1 m_t$, $\tilde{m}_W = 80.4$ GeV and $\tilde{m}_t = 172.5$ GeV. The values of σ_{m_W} and σ_{m_t} reflect the dijet mass resolution. If either dijet in an event has $X_{tt} < 3.2$ for any possible combination with an extra jet, the event is rejected. This requirement reduces the $t\bar{t}$ background by ~60%, whilst retaining ~90% of signal events. Note that no lepton veto is used in the event selection.

---

[3]Proton-proton collision vertices are reconstructed in ATLAS by requiring that at least five tracks with $p_T > 0.4$ GeV be associated to a given vertex. If multiple vertices are reconstructed within one event, the primary vertex is taken to be the vertex with the highest summed track p_T^2.

[4]A jet is labelled as a b-jet if a b-hadron with transverse momentum above 5 GeV exists within a cone of $\Delta R = 0.3$ from the jet axis.
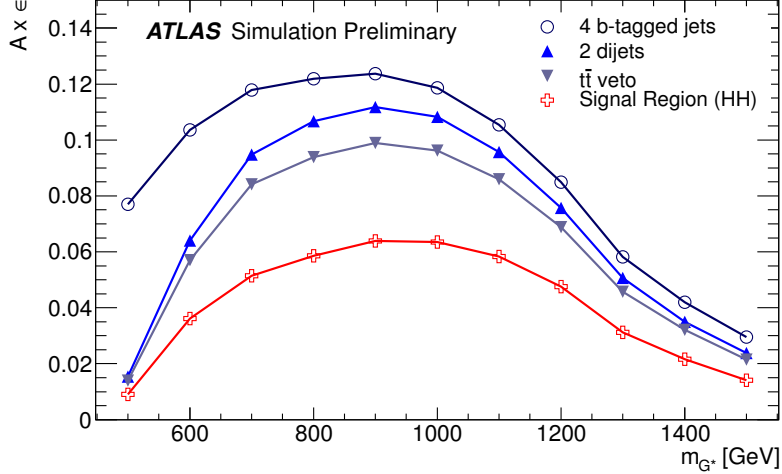
Figure 1: The acceptance $\times$ efficiency ($A \times \epsilon$) for $G^* \to HH \to b\bar{b}b\bar{b}$ events at each stage of the event selection for each of the G^* MC samples. Correction factors have been applied to account for the differences observed in the b-tagging efficiency for b-jets in data and MC simulation [20].

The event selection criteria described above are collectively referred to as the "4-tag" selection requirements. After these requirements, 2357 events are selected. A significant further reduction of the backgrounds is achieved by requiring that the masses of the two dijets are compatible with the HH hypothesis. A "Signal Region" is defined by making an elliptical cut in the plane of leading dijet[5] invariant mass, $m_{\text{dijet}}^{\text{lead}}$, and sub-leading dijet invariant mass, $m_{\text{dijet}}^{\text{subl}}$:

$$X_{HH} = \sqrt{\left(\frac{m_{\text{dijet}}^{\text{lead}} - \tilde{m}_{\text{dijet}}^{\text{lead}}}{\sigma_{m_{\text{dijet}}^{\text{lead}}}}\right)^2 + \left(\frac{m_{\text{dijet}}^{\text{subl}} - \tilde{m}_{\text{dijet}}^{\text{subl}}}{\sigma_{m_{\text{dijet}}^{\text{subl}}}}\right)^2}, \tag{1}$$

where $\sigma_{m_{\text{dijet}}^{\text{lead}}} = 0.1 m_{\text{dijet}}^{\text{lead}}$, $\sigma_{m_{\text{dijet}}^{\text{subl}}} = 0.1 m_{\text{dijet}}^{\text{subl}}$, $\tilde{m}_{\text{dijet}}^{\text{lead}} = 124.0\,\text{GeV}$ and $\tilde{m}_{\text{dijet}}^{\text{subl}} = 115.0\,\text{GeV}$. The values of $\tilde{m}_{\text{dijet}}^{\text{lead}}$ and $\tilde{m}_{\text{dijet}}^{\text{subl}}$ are determined using the signal MC samples, and again the values of $\sigma_{m_{\text{dijet}}^{\text{lead}}}$ and $\sigma_{m_{\text{dijet}}^{\text{subl}}}$ reflect the dijet mass resolution. The requirement $X_{HH} < 1.6$ defines the Signal Region. It rejects $\sim$95% of the background events that satisfy the selection requirements up to this point, keeping $\sim$65% of the signal events. The choice of $\tilde{m}_{\text{dijet}}^{\text{subl}} < \tilde{m}_{\text{dijet}}^{\text{lead}}$ is motivated by the increased likelihood of radiative energy losses and semi-leptonic decays for the sub-leading dijet. The data contains 114 events within the Signal Region, although this data was not examined ("blinded") until the background prediction and its associated uncertainties were fully defined. Whilst blinded, the above event selection criteria were optimised to give the best expected sensitivity to $G^* \to HH \to b\bar{b}b\bar{b}$ in the m_{G^*} range considered.

Figure 1 shows the acceptance $\times$ efficiency ($A \times \epsilon$) at each stage of the event selection for each of the G^* MC samples. For G^* masses between 700 and 1200 GeV the $A \times \epsilon$ after the full Signal Region selection requirements is between 5% and 7%. The $A \times \epsilon$ is lower for lower m_{G^*} as a result of the high $p_{\text{T}}^{\text{dijet}}$ requirement and the individual jet p_{T} requirement. At higher m_{G^*} the Higgs bosons are produced with a high enough p_{T} that it becomes difficult to resolve each Higgs boson as two separate anti-k_{t} $R=0.4$ jets, and there is thus a significant inefficiency in the 4 b-tagged jets requirement.

---

[5]The leading dijet is that with the highest $p_{\text{T}}^{\text{dijet}}$.

6 Background Modelling

After the 4-tag selection requirements described above have been applied about 90% of the total background in the Signal Region arises from multijet events. Both the m_{4j} shape and the normalisation of the multijet background are determined from data. The remaining ∼10% of background are $t\bar{t}$ events. The $t\bar{t}$ yield is determined from data, while the m_{4j} shape is taken from MC simulation. A Z+jets contribution comprising < 1% of the total background is modelled using MC simulation. The contribution from Higgs production in association with $t\bar{t}$ is negligible.

6.1 Multijet Background

The multijet background is modelled using an independent data sample that is selected using the same trigger and selection requirements as described in Section 5, except for the b-tagging requirement: only one of the two selected dijets is required to be formed from b-tagged jets, the other dijet can be formed from jets which need not pass the b-tagging requirement. This is referred to hereafter as the "2-tag" selection and data sample. It comprises 336340 events, with negligible signal contamination, 98% of which are multijet events (estimated using the predicted yield of the $t\bar{t}$ MC sample in the 2-tag selection). The event yield and m_{4j} distribution of this 2-tag sample are used to predict the multijet background in the 4-tag data. However, this 2-tag sample first has to be normalised and its kinematics adjusted before a reliable multijet background prediction can be produced. This is done by comparison to the 4-tag data in a signal-free Sideband Region of the $m_{\text{dijet}}^{\text{lead}}$-$m_{\text{dijet}}^{\text{subl}}$ plane, defined as follows:

- Sideband Region: NOT ((60 GeV < $m_{\text{dijet}}^{\text{subl}}$ < 160 GeV) AND (60 GeV < $m_{\text{dijet}}^{\text{lead}}$ < 160 GeV)).

In addition, an orthogonal Control Region is used to test the multijet modelling description, and defined as follows:

- Control Region: NOT (Sideband Region) AND NOT (Signal Region OR ZZ Region OR ZH Region),

where the ZZ and ZH Regions are regions of the $m_{\text{dijet}}^{\text{lead}}$-$m_{\text{dijet}}^{\text{subl}}$ plane where one could potentially be sensitive to $X \rightarrow ZZ \rightarrow b\bar{b}b\bar{b}$ or $X \rightarrow ZH \rightarrow b\bar{b}b\bar{b}$ signals, and are defined using elliptical cuts as for the Signal Region (Equation 1), but with small modifications of the parameters. The ZZ Region is defined using $\tilde{m}_{\text{dijet}}^{\text{lead}}$ = 93.0 GeV, $\tilde{m}_{\text{dijet}}^{\text{subl}}$ = 86.0 GeV and X_{ZZ} < 1.5, and the two ZH Regions (corresponding to the leading dijet being consistent with the H and the sub-leading dijet being consistent with the Z, and vice versa) are defined using $\tilde{m}_{\text{dijet}}^{\text{lead}}$ = 124.0 (93.0) GeV, $\tilde{m}_{\text{dijet}}^{\text{subl}}$ = 86.0 (115.0) GeV, with $X_{HZ(ZH)}$ < 1.6. These regions are excluded, along with the Signal Region, so that the Control Region remains relatively free of potential resonant diboson contamination. The Sideband and Control Regions are shown in Figure 2. Events in the 4-tag data sample, 2-tag data sample, $t\bar{t}$ MC and Z+jets MC are categorised as being either in the Sideband Region, the Control Region or the Signal Region.

The Sideband Region of the 4-tag sample is 97% pure in multijet events (estimated using the predicted $t\bar{t}$ and Z+jets yields), and can thus be used to determine the normalisation of the multijet background, with minimal input from simulation, as follows. In each of the Sideband, Control and Signal Regions the event yield in the 2-tag data sample is scaled using a common factor, μ_{multijet}, defined as:

$$\mu_{\text{multijet}} = \frac{N_{4-\text{tag}}^{\text{Sideband}} - N_{t\bar{t},4-\text{tag}}^{\text{Sideband}} - N_{Z+\text{jets},4-\text{tag}}^{\text{Sideband}}}{N_{2-\text{tag}}^{\text{Sideband}}}, \tag{2}$$

where $N_{4-\text{tag}}^{\text{Sideband}}$ is the number of events in the Sideband Region in the 4-tag data sample, $N_{t\bar{t},4-\text{tag}}^{\text{Sideband}}$ the number of $t\bar{t}$ events in the 4-tag Sideband Region, as predicted by the data-driven $t\bar{t}$ method described in
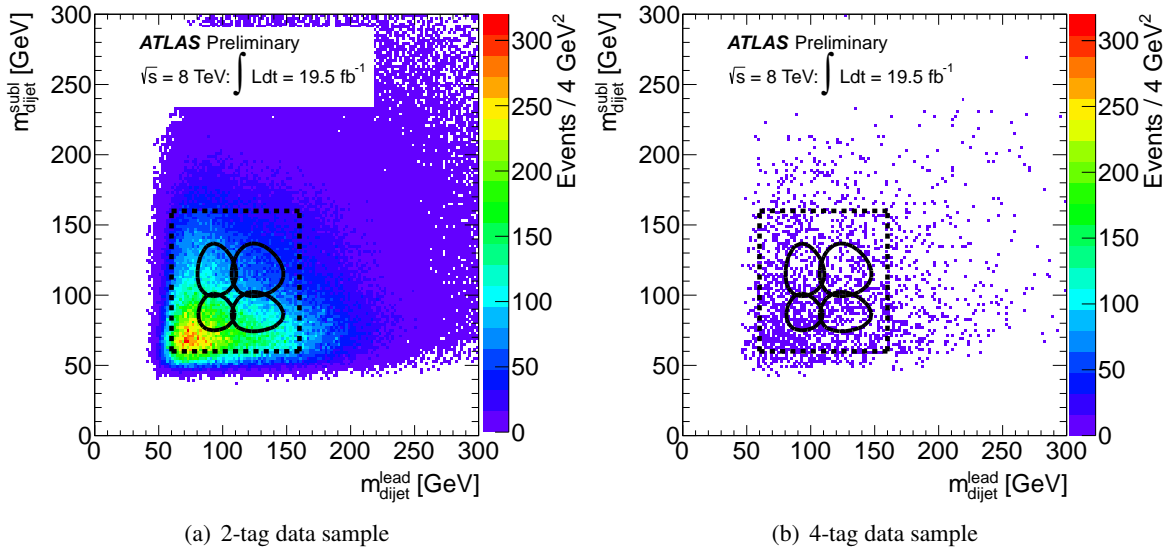
(a) 2-tag data sample

(b) 4-tag data sample

Figure 2: The distribution of events in the m_{dijet}^{lead}-m_{dijet}^{subl} plane for the 2-tag data sample (left) and the 4-tag data sample (right). The Sideband Region is that region outside of the dashed-line box. The four overlapping ellipses of the Signal, *ZZ* and *ZH* Regions are shown with solid lines. The Control Region is that region enclosed by the dashed-line box but outside of the Signal, *ZZ* and *ZH* Regions.

the next section, $N_{Z+jets,4-tag}^{Sideband}$ the number of Z+jets events in the 4-tag Sideband Region predicted by the Z+jets MC, and $N_{2-tag}^{Sideband}$ is the number of events in the Sideband Region in the 2-tag data sample. This gives $\mu_{multijet} = 0.0064 \pm 0.0002$. In this way, the multijet background prediction is scaled such that the total number of background events equals the number of events in the 4-tag data sample in the Sideband Region. This can be seen in Table 1, where the predicted and observed event yields in the Sideband Region and Control Region are compared.

The 4-tag data sample in the Sideband Region is also used to refine the kinematics of the multijet background prediction via a reweighting of the events in the 2-tag sample. The loosened *b*-tagging requirements of the 2-tag sample result in biases with respect to the multijet background in the 4-tag sample, as shown in Figure 3(a) for the m_{4j} distribution. To correct for these biases the events of the 2-tag sample are reweighted using weights that are determined by taking the ratio of the 2-tag and 4-tag data distributions in the Sideband Region of the following kinematic variables:

- The leading dijet p_T.

- The ΔR separation of the jets in the sub-leading dijet.

- The ΔR separation of the dijets.

These are the variables which exhibit the largest discrepancy between the 2-tag and 4-tag samples. The reweighting is iterated five times, after which there is exact agreement between the 2-tag and 4-tag distributions in all three variables. The weights are constructed such that the total number of events in the 2-tag sample remains unchanged. Figure 3(b) shows how the reweighting corrects the m_{4j} distribution of the 2-tag sample in the Sideband Region. Note that, whilst the weights themselves are determined using the Sideband Region distributions, the same weights are applied to all events in order to correct the kinematics in all regions.

Type	Sideband Region	Control Region
Multijet	903 ± 3	935 ± 3
$t\bar{t}$	19.0 ± 0.2	26.7 ± 0.3
Z+jets	11 ± 1	17 ± 1
Total Bkgd	933 ± 3	979 ± 3
4-tag Data	933	933
G^* (m_{G^*} = 500 GeV)	0.75 ± 0.10	3.9 ± 0.2
G^* (m_{G^*} = 700 GeV)	0.48 ± 0.04	3.0 ± 0.1

Table 1: The expected event yields and the observed event yield in data after the 4-tag selection in the Sideband Region and Control Region, and the predicted G^* signal yield in these regions for two different values of m_{G^*}. The uncertainties shown are statistical only. The $t\bar{t}$ prediction is determined using the data-driven method described in Section 6.2, whereas the small Z+jets background is taken from MC. By coincidence, the observed event yield in the data is exactly the same for the Sideband and Control Regions.

(a) Sideband Region: Before reweighting
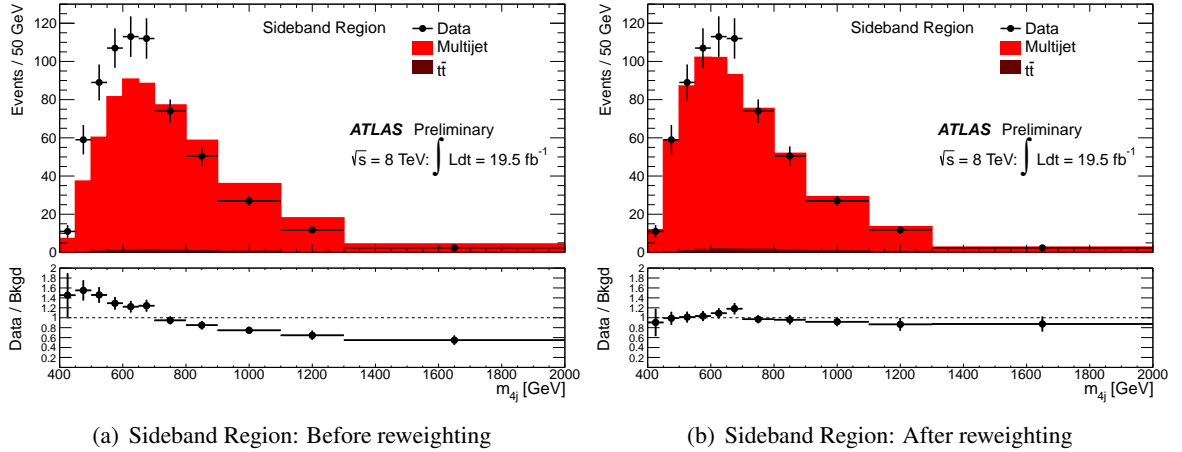

(b) Sideband Region: After reweighting

Figure 3: A comparison of the predicted m_{4j} background distribution to that observed in the 4-tag data in the Sideband Region, before and after reweighting of the 2-tag multijet background model to the 4-tag data in the Sideband Region. The multijet and $t\bar{t}$ background contributions are shown as stacked histograms. In both cases the 2-tag multijet background has been scaled using μ_{multijet} (Equation 2). The negligible Z+jets background contribution is not shown.
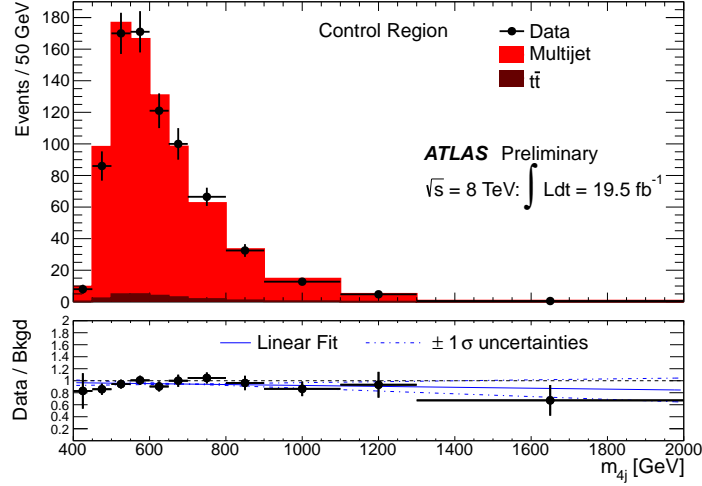
Figure 4: A comparison of the predicted m_{4j} background distribution to that observed in the 4-tag data in the Control Region. The multijet and $t\bar{t}$ background contributions are shown as stacked histograms. The negligible Z+jets background contribution is not shown. In the bottom panel the straight line fit to the ratio of the distributions is shown, along with the uncertainties on this fit, which are used to determine the multijet background shape uncertainty.

The Control Region also has a very high multijet event content (96%), and can therefore be used to test both the normalisation and the m_{4j} shape of the multijet background predicted by the reweighted 2-tag model, and the results of this test used to estimate the uncertainties on the multijet background in the Signal Region. Table 1 shows that the prediction for the total number of background events in the Control Region is in agreement with the observed number in the 4-tag data sample at the level of 5%. This difference is propagated as a systematic uncertainty on the normalisation of the multijet background in the Signal Region. Figure 4 shows a comparison of the m_{4j} distribution of the total background prediction to the 4-tag data in the Control Region. Good agreement in the shape is observed, and a straight line fit to the ratio of the distributions gives a slope m consistent with zero to within the $\pm 1\sigma$ uncertainties on the slope $\pm \delta m$. This fit, along with its uncertainties, is shown in the bottom panel of Figure 4. The uncertainties on the fitted slope are used to bound the m_{4j} shape uncertainty on the multijet background. A new straight line function with slope m' is defined, where $m' = m + \delta m$ or $m' = |m - \delta m|$, whichever gives the largest $|m'|$. This function defines the "positive" shape uncertainty on the multijet background m_{4j} shape, with the "negative" shape uncertainty defined as the reflection of this function in the line y=1.0. The uncertainty is 7% at $m_{4j} = 400$ GeV, and 15% at $m_{4j} = 1500$ GeV.

Several cross-checks of the data-driven multijet background prediction are made. The exact definitions of the Sideband Region and Control Regions are varied, such that the regions become more or less dominated by events with predominantly higher or lower dijet masses. In addition, the b-tagging requirements of the two b-tagged jets in the 2-tag sample are varied to produce a sample with varying b-jet purity. In all cases, the multijet background prediction in the Signal Region is consistent, both in terms of shape and normalisation, to within the uncertainties defined above.

6.2 $t\bar{t}$ Background

Events in which a pair of top quarks are produced in the hard scatter are a background for this analysis when one of the W decay products, typically a charm quark, is mistakenly b-tagged, and the resulting

system passes the $t\bar{t}$ veto. In addition, losing a jet from a hadronically decaying top quark can lead to a dijet system with mass near m_h. A data-driven prediction for the $t\bar{t}$ background normalisation is employed, as the simulation may not accurately model the $t\bar{t}$ selection efficiency.

The number of $t\bar{t}$ background events is predicted using a "$t\bar{t}$ Control Region", defined by reversing the $t\bar{t}$ veto described in Section 5. Events in which one or both of the reconstructed dijets fail the $t\bar{t}$ veto, but pass all the other 4-tag selection criteria, are selected, giving a data yield of 47 events. The multijet contribution to this region is estimated using a "2-tag" data sample that is constructed as described in Section 6.1, with the exception that one or both of the dijets fail the $t\bar{t}$ veto. In order to correct for the additional inefficiencies of the 4-tag selection, the yield of the 2-tag sample is scaled using the same μ_{multijet} factor of Equation 2, to give the multijet prediction. After multijet background subtraction, the number of $t\bar{t}$ events in the $t\bar{t}$ Control Region, $N_{t\bar{t}}^{CR}$, is estimated to be 16 ± 7, where the uncertainty is dominated by the statistical uncertainty on the limited data yield in the region.

This yield is then extrapolated to give the predicted $t\bar{t}$ yield in the Signal Region, $N_{t\bar{t}}^{Bkg}$, using the following equation:

$$N_{t\bar{t}}^{Bkg} = \frac{\epsilon_{t\bar{t}}^2}{1 - \epsilon_{t\bar{t}}^2} \times N_{t\bar{t}}^{CR}, \qquad (3)$$

where $\epsilon_{t\bar{t}}$ is the efficiency for a selected dijet in a $t\bar{t}$ event to pass the $t\bar{t}$ veto. This equation relies on the assumption that the $\epsilon_{t\bar{t}}$ of each dijet in the event are uncorrelated, and this is validated in $t\bar{t}$ MC. The $\epsilon_{t\bar{t}}$ is measured using an independent "leptonic $t\bar{t}$" data sample that has a high $t\bar{t}$ purity. Events in this sample are selected by requiring one dijet candidate, defined using 2 b-tagged jets as described in Section 5, and one "leptonic top-quark" candidate. The leptonic top-quark candidate is defined using a reconstructed muon and one b-tagged jet. This b-tagged jet is required to be distinct from jets in the dijet candidate, and the muon is required to have $p_{\text{T}} > 25\,\text{GeV}$, to be well isolated, and to fall within $\Delta R < 1.2$ of the b-tagged jet. The leptonic top candidate is required to have $p_{\text{T}} > 200\,\text{GeV}$, where the leptonic top $\vec{p}_T$ is defined as the vector sum of the b-jet $\vec{p}_T$, the muon $\vec{p}_T$, and the missing E_{T}. No other requirement on missing E_{T} is made. The $t\bar{t}$ veto efficiency is then measured as the fraction of the reconstructed dijet candidates passing the $t\bar{t}$ veto, giving $\epsilon_{t\bar{t}} = 0.62 \pm 0.04\,\text{(stat.)} \pm 0.06\,\text{(sys.)}$. A 10% systematic uncertainty is assigned to cover potential differences between $\epsilon_{t\bar{t}}$ as measured in the leptonic $t\bar{t}$ sample, and $\epsilon_{t\bar{t}}$ in the full 4-tag selection, applying the method in $t\bar{t}$ MC to evaluate such differences. The measured $\epsilon_{t\bar{t}}$ agrees well with the corresponding semi-leptonic $t\bar{t}$ MC prediction of 0.60.

Combining the measurements of $N_{t\bar{t}}^{CR}$ and $\epsilon_{t\bar{t}}$ using Equation 3 gives a data-driven $t\bar{t}$ background prediction of 10 ± 6 events in the Signal Region. The uncertainty is dominated by the statistical uncertainty on $N_{t\bar{t}}^{CR}$, with a smaller contribution from the uncertainty on $\epsilon_{t\bar{t}}$. This data-driven $t\bar{t}$ background prediction is consistent with the MC prediction of 14.3 events.

Due to the limited statistics in the $t\bar{t}$ Control Region, the $m_{4\text{j}}$ shape of the $t\bar{t}$ background has to be modelled using MC simulation. In order to increase the statistical precision of the shape description, the $t\bar{t}$ shape is derived from MC simulation using the "2-tag" selection, described in Section 6.1. A systematic uncertainty on the $t\bar{t}$ $m_{4\text{j}}$ shape is derived by comparing the 2-tag and 4-tag $m_{4\text{j}}$ distributions in MC simulation. A straight line fit to the ratio of the normalized distributions is made, and this fit used to define the shape uncertainty using the same prescription as described for the multijet shape uncertainty in Section 6.1. The uncertainty is 27% at $m_{4\text{j}} = 400$ GeV, and 60% at $m_{4\text{j}} = 1500$ GeV.

7 Systematic Uncertainties

The following sources of systematic uncertainty that affect only the background prediction are considered:

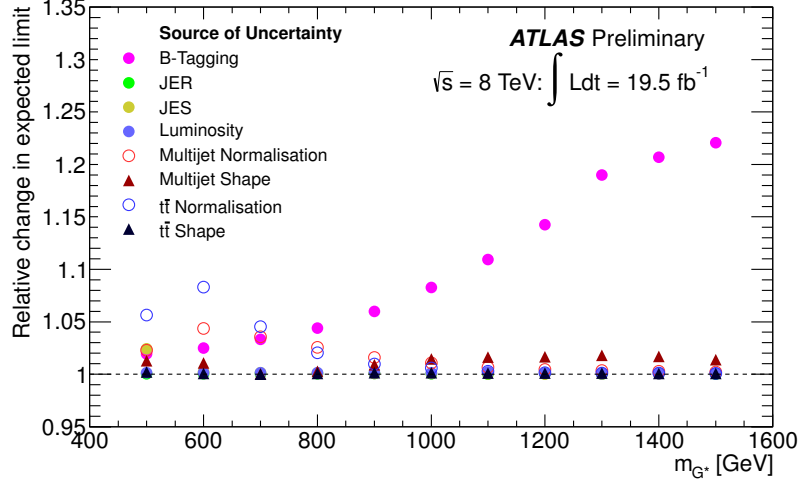- Multijet background normalisation (5% uncertainty).

Figure 5: The individual relative impact on the expected $\sigma(pp \rightarrow G^*) \times \mathrm{BR}(G^* \rightarrow HH \rightarrow b\bar{b}b\bar{b})$ limit from each of the systematic sources considered in the analysis, as a function of the G^* mass.

- Multijet background shape (7–15% uncertainty).

- $t\bar{t}$ background normalisation (59% uncertainty).

- $t\bar{t}$ background shape (27–60% uncertainty).

The derivation of these uncertainties is described in the previous section. Additionally, to account for limitations of the ATLAS detector simulation, the following uncertainties on the MC simulated signal are considered:

- Jet energy scale (JES) uncertainties.

- Jet energy resolution (JER) uncertainties.

- Uncertainties in the efficiency for b-jets to be b-tagged.

The JES systematic uncertainty is evaluated using 17 separate and orthogonal uncertainty components, which allow for the correct treatment of correlations across the kinematic bins [47–49]. The JER uncertainty is evaluated by smearing jet energies according to the systematic uncertainties of the resolution measurement performed with data [50]. For b-jets with $p_T < 300$ GeV the uncertainty on the b-tagging efficiency is evaluated by propagating the systematic uncertainty on the measured tagging efficiency for b-jets [20]. However, for the higher G^* masses considered in this analysis, there are a significant number of events containing at least one b-jet with $p_T > 300$ GeV. In this kinematic region, the systematic uncertainty on the tagging efficiency is derived from MC simulation. These high-p_T uncertainties range from 12% to 33%, and are validated by comparing the b-tagging rate between data and MC in samples of inclusive jet production.

Figure 5 shows the relative impact on the expected $\sigma(pp \rightarrow G^*) \times \mathrm{BR}(G^* \rightarrow HH \rightarrow b\bar{b}b\bar{b})$ limit of each of the systematic uncertainty sources. The construction of the expected limit itself is described in the next section. One can see that for $m_{G^*} < 800$ GeV, the $t\bar{t}$ and multijet normalisation uncertainties are important, but at higher masses the impact on the limit is dominated by the b-tagging uncertainties affecting the signal prediction, in particular the high-p_T b-tagging uncertainties for jets with $p_T > 300$ GeV. The JES uncertainty is only important for $m_{G^*} = 500$ GeV, since for this mass point the jet p_T spectrum is

Type	Signal Region
Multijet	109 ± 5
$t\bar{t}$	10 ± 6
Z+jets	0.7 ± 0.2
Total Bkgd	120 ± 8
Data	114
G^* (m_{G^*} = 500 GeV)	12.5 ± 0.4
G^* (m_{G^*} = 700 GeV)	12.5 ± 0.2

Table 2: The expected event yield in the Signal Region for each of the background sources considered, the total expected background, the number of observed events in the data, and the predicted G^* signal yield for two different values of m_{G^*}. The statistical plus systematic uncertainty on the data-driven multijet and $t\bar{t}$ backgrounds are shown. The small Z+jets background is estimated using MC simulation, and the uncertainty is statistical only. The uncertainty on the signal yields is statistical only. The similarity in the signal yields for the two different m_{G^*} values is due to the fact that, whilst the G^* production cross-section decreases with m_{G^*}, the A $\times$ ϵ sharply increases (as shown in Figure 1).

soft enough that migrations across the jet $p_\text{T} > 40$ GeV and $p_\text{T}^\text{dijet} > 200$ GeV thresholds from JES variations are significant. The uncertainties on the multijet and $t\bar{t}$ background shapes do not have a significant impact on the expected sensitivity.

8   Results and Interpretation

Table 2 shows the predicted number of events in the Signal Region for each of the background sources considered, the total background, the number of observed events in the data, and the predicted G^* signal yield for two different values of m_{G^*}. The numbers of predicted and observed events are consistent. Figure 6 shows a comparison of the predicted m_4j background distribution to that observed in the data. The predicted and observed distributions are in good agreement.

The statistical procedure used to interpret the data is the one described in Ref. [15] and references therein. Hypothesised values of μ, the global signal strength factor, are tested with a test statistic based on the profile likelihood ratio [51]. In the profile likelihoods, the maximum likelihood values are obtained with the systematic uncertainties treated as independent, Gaussian or log-normal constraint terms. First, a statistical test of the background-only hypothesis ($\mu = 0$) is carried out, in order to determine if there are any statistically significant local excesses in the data. The significance of an excess is quantified using the local p_0, the probability that the background can produce a fluctuation greater than or equal to the excess observed in data. Expressed in terms of standard deviations, no local p_0 with a significance greater than 1σ is observed, with a maximum significance of 1σ being observed for the $m_{G^*} = 500$ GeV and $m_{G^*} = 800$ GeV signal mass points.

Given that there is no evidence of a signal, the result is used to set upper limits on $\sigma(pp \rightarrow G^*) \times$
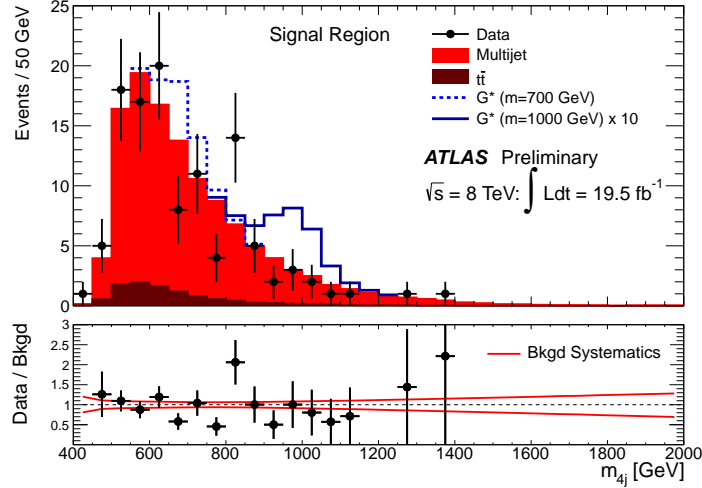
Figure 6: A comparison of the predicted m_{4j} background distribution to that observed in the data in the Signal Region. The multijet and $t\bar{t}$ background contributions are shown as stacked histograms. The negligible Z+jets background contribution is not shown. Additionally, the predicted m_{4j} distributions of two G^* signal samples with $m_{G^*} = 700$ GeV and $m_{G^*} = 1$ TeV are shown, stacked on top of the predicted background. The $m_{G^*} = 700$ GeV sample is normalised using the predicted cross-section of the model, whereas the cross-section used to normalize the $m_{G^*} = 1$ TeV sample has been increased by a factor ten from that predicted by the model. In the bottom panel, the ratio of the data to the background distribution is shown, along with a band displaying the total systematic error on the background prediction.

BR($G^* \rightarrow HH \rightarrow b\bar{b}b\bar{b}$), as a function of m_{G^*}. Exclusion limits are based on the value of the statistic CL_s [52], with a value of μ regarded as excluded at 95% confidence level (CL) when CL_s is less than 5%. The asymptotic approximation [51], upon which the results are based, has been validated using pseudo-experiments.

Figure 7 shows the expected and observed limits on $\sigma(pp \rightarrow G^*) \times$ BR($G^* \rightarrow HH \rightarrow b\bar{b}b\bar{b}$) as a function of m_{G^*}. The observed limit at the 95% CL ranges between 100 fb at 500 GeV and 7 fb at 1 TeV. The KK Graviton used as a benchmark in this study is excluded at the 95% CL for m_{G^*} between 590 GeV and 710 GeV, using a linear interpolation of the limit between the mass points. The expected exclusion range is 590-630 GeV.

9 Conclusions

The results of the search for resonant di-Higgs production, $X \rightarrow HH \rightarrow b\bar{b}b\bar{b}$, are presented for resonance masses between 500 GeV and 1.5 TeV. The observed data are compatible with the background-only prediction across the full mass range probed, and no evidence for a new resonance is found. The results are interpreted in terms of a spin-2 KK graviton decaying to HH in the bulk RS model, with $k/\bar{M}_{Pl} = 1.0$. The observed upper limit on $\sigma(pp \rightarrow G^*) \times$ BR($G^* \rightarrow HH \rightarrow b\bar{b}b\bar{b}$) at the 95% CL ranges from 100 fb at 500 GeV to 7 fb at 1 TeV, demonstrating the good level of sensitivity available in this channel to $X \rightarrow HH \rightarrow b\bar{b}b\bar{b}$. The model is excluded at the 95% CL for m_{G^*} between 590 GeV and 710 GeV.
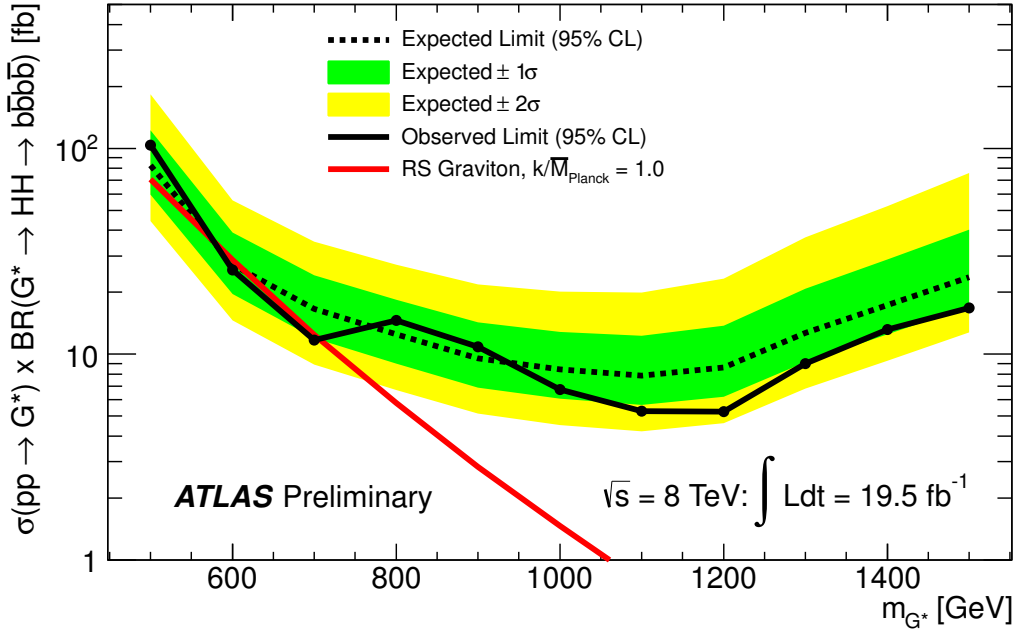
Figure 7: The expected and observed 95% CL upper limits on $\sigma(pp \to G^*) \times BR(G^* \to HH \to b\bar{b}b\bar{b})$ as a function of m_{G^*}. The dashed line shows the expected limit, and the solid line the observed limit, using a linear interpolation between the mass points. The inner and outer bands on the expected limit represent $\pm 1\sigma$ and $\pm 2\sigma$ variations, respectively. Also shown is the leading-order prediction for $\sigma(pp \to G^*) \times BR(G^* \to HH \to b\bar{b}b\bar{b})$ as a function of m_{G^*} in the bulk RS model with $k/\bar{M}_{Pl} = 1.0$.

References

[1] G. Altarelli, B. Mele, and M. Ruiz-Altaba, *Searching for New Heavy Vector Bosons in $p\bar{p}$ Colliders*, Z.Phys. **C45** (1989) 109.

[2] E. Eichten and K. Lane, *Low-scale technicolor at the Tevatron and LHC*, Phys.Lett. **B669** (2008) 235–238, `arXiv:0706.2339 [hep-ph]`.

[3] L. Randall and R. Sundrum, *A Large mass hierarchy from a small extra dimension*, Phys.Rev.Lett. **83** (1999) 3370–3373.

[4] K. Agashe, H. Davoudiasl, G. Perez, and A. Soni, *Warped Gravitons at the LHC and Beyond*, Phys.Rev. **D76** (2007) 036006, `arXiv:hep-ph/0701186 [hep-ph]`.

[5] G. M. Pruna and T. Robens, *The Higgs Singlet extension parameter space in the light of the LHC discovery*, Phys.Rev. **D88** (2013) 115012, `arXiv:1303.1150 [hep-ph]`.

[6] B. Coleppa, F. Kling, and S. Su, *Constraining Type II 2HDM in Light of LHC Higgs Searches*, `arXiv:1305.0002 [hep-ph]`.

[7] ATLAS Collaboration, *Search for resonant ZZ production in the $ZZ \to \ell\ell qq$ channel with the ATLAS detector using $7.2\,fb^{-1}$ of $\sqrt{s} = 8\,TeV\,pp$ collision data*, ATLAS-CONF-2012-150 . `https://cds.cern.ch/record/1493489`.

[8] CMS Collaboration, *Search for a narrow spin-2 resonance decaying to Z bosons in the semileptonic final state*, CMS-PAS-EXO-12-022 . `https://cds.cern.ch/record/1596494`.

[9] ATLAS Collaboration, *Search for resonant diboson production in the lvjj decay channels with the ATLAS detector at 7 TeV*, Phys.Rev. **D87** (2013) 112006, `arXiv:1305.0125 [hep-ex]`.

[10] CMS Collaboration, *Search for new resonances decaying to $WW \to \ell\nu qq$ in the final state with a lepton, missing transverse energy, and single reconstructed jet*, CMS PAS EXO-12-021 . `https://cds.cern.ch/record/1590301`.

[11] ATLAS Collaboration, *Search for resonant $WZ \to \ell\nu\ell\ell$ production using $\sqrt{s} = 8\,TeV\,pp$ collisions with ATLAS*, ATLAS-CONF-2013-015 . `https://cds.cern.ch/record/1525522`.

[12] CMS Collaboration, *Search for a W' or Techni-ρ Decaying into WZ in pp Collisions at $\sqrt{s} = 7\,TeV$*, Phys.Rev.Lett. **109** (2012) 141801, `arXiv:1206.0433 [hep-ex]`.

[13] CMS Collaboration, *Search for exotic resonances decaying into WZ/ZZ in pp collisions at $\sqrt{s} = 7\,TeV$*, JHEP **1302** (2013) 036, `arXiv:1211.5779 [hep-ex]`.

[14] CMS Collaboration, *Search for heavy resonances in the W/Z-tagged dijet mass spectrum in pp collisions at 7 TeV*, Phys.Lett. **B723** (2013) 280–301.

[15] ATLAS Collaboration, *Observation of a new particle in the search for the Standard Model Higgs boson with the ATLAS detector at the LHC*, Phys.Lett. **B716** (2012) 1–29, `arXiv:1207.7214 [hep-ex]`.

[16] CMS Collaboration, *Observation of a new boson at a mass of 125 GeV with the CMS experiment at the LHC*, Phys.Lett. **B716** (2012) 30–61, `arXiv:1207.7235 [hep-ex]`.

[17] CMS Collaboration, *Search for extended Higgs sectors in the H → hh and A → Zh channels in* $\sqrt{s}$ = 8 *TeV pp collisions with multileptons and photons final states*, CMS-PAS-HIG-13-025 . https://cds.cern.ch/record/1637776.

[18] B. Cooper, N. Konstantinidis, L. Lambourne, and D. Wardrope, *Boosted hh → b$\bar{b}$b$\bar{b}$: A new topology in searches for TeV-scale resonances at the LHC*, Phys.Rev. **D88** 114005.

[19] M. Cacciari, G. P. Salam, and G. Soyez, *The anti-k_t jet clustering algorithm*, JHEP **0804** (2008) 063.

[20] ATLAS Collaboration, *Measuring the b-tag efficiency in a top-pair sample with 4.7 fb^{-1} of data from the ATLAS detector*, ATLAS-CONF-2012-097 . https://cds.cern.ch/record/1460443.

[21] A. L. Fitzpatrick, J. Kaplan, L. Randall, and L.-T. Wang, *Searching for the Kaluza-Klein Graviton in Bulk RS Models*, JHEP **0709** (2007) 013, arXiv:hep-ph/0701150 [hep-ph].

[22] ATLAS Collaboration, *The ATLAS Experiment at the CERN Large Hadron Collider*, JINST **3** (2008) S08003.

[23] ATLAS Collaboration, *Improved luminosity determination in pp collisions at* $\sqrt{s}$ = 7 *TeV using the ATLAS detector at the LHC*, Eur.Phys.J. **C73** (2013) 2518.

[24] J. Alwall et al., *MadGraph 5 : Going Beyond*, JHEP **1106** (2011) 128.

[25] T. Sjostrand, S. Mrenna, and P. Z. Skands, *A Brief Introduction to PYTHIA 8.1*, Comput.Phys.Commun. **178** (2008) 852–867.

[26] LHC Higgs Cross Section Working Group Collaboration, S. Heinemeyer et al., *Handbook of LHC Higgs Cross Sections: 3. Higgs Properties*, arXiv:1307.1347 [hep-ph].

[27] D. Stump, J. Huston, J. Pumplin, W.-K. Tung, H. Lai, et al., *Inclusive jet production, parton distributions, and the search for new physics*, JHEP **0310** (2003) 046.

[28] P. Nason, *A New method for combining NLO QCD with shower Monte Carlo algorithms*, JHEP **0411** (2004) 040, arXiv:hep-ph/0409146 [hep-ph].

[29] S. Frixione, P. Nason, and C. Oleari, *Matching NLO QCD computations with Parton Shower simulations: the POWHEG method*, JHEP **0711** (2007) 070, arXiv:0709.2092 [hep-ph].

[30] H.-L. Lai et al., *New parton distributions for collider physics*, Phys.Rev. **D82** (2010) 074024.

[31] M. Cacciari et al., *Top-pair production at hadron colliders with next-to-next-to-leading logarithmic soft-gluon resummation*, Phys.Lett. **B710** (2012) 612–622.

[32] P. Bärnreuther, M. Czakon, and A. Mitov, *Percent Level Precision Physics at the Tevatron: First Genuine NNLO QCD Corrections to q$\bar{q}$ → t$\bar{t}$ + X*, Phys.Rev.Lett. **109** (2012) 132001.

[33] M. Czakon and A. Mitov, *NNLO corrections to top-pair production at hadron colliders: the all-fermionic scattering channels*, JHEP **1212** (2012) 054.

[34] M. Czakon and A. Mitov, *NNLO corrections to top pair production at hadron colliders: the quark-gluon reaction*, JHEP **1301** (2013) 080.

[35] M. Czakon, P. Fiedler, and A. Mitov, *The total top quark pair production cross-section at hadron colliders through $O(\alpha_S^4)$*, Phys.Rev.Lett. **110** (2013) 252004.

[36] M. Czakon and A. Mitov, *Top++: A Program for the Calculation of the Top-Pair Cross-Section at Hadron Colliders*, arXiv:1112.5675 [hep-ph].

[37] S. Agostinelli et al., *G4 – a simulation toolkit*, Nucl. Instrum. Meth. **A506** (2003) 250.

[38] ATLAS Collaboration, *The ATLAS Simulation Infrastructure*, Eur. Phys. J. **C70** (2010) 823–874.

[39] ATLAS Collaboration, *Fast Simulation for ATLAS: Atlfast-II and ISF*, J.Phys.Conf.Ser. **396** (2012) 022031.

[40] ATLAS Collaboration, *The simulation principle and performance of the ATLAS fast calorimeter simulation FastCaloSim*, ATL-PHYS-PUB-2010-013 . https://cds.cern.ch/record/1300517.

[41] ATLAS Collaboration, *Jet energy measurement with the ATLAS detector in proton-proton collisions at $\sqrt{s} = 7\,TeV$*, Eur.Phys.J. **C73** (2013) 2304.

[42] M. Cacciari, G. P. Salam, and G. Soyez, *The Catchment Area of Jets*, JHEP **0804** (2008) 005.

[43] ATLAS Collaboration, *Muon reconstruction efficiency in reprocessed 2010 LHC proton-proton collision data recorded with the ATLAS detector*, ATLAS-CONF-2011-063 . https://cds.cern.ch/record/1345743.

[44] ATLAS Collaboration, *Pile-up subtraction and suppression for jets in ATLAS*, ATLAS-CONF-2013-083 . https://cds.cern.ch/record/1570994.

[45] ATLAS Collaboration, *Selection of jets produced in proton-proton collisions with the ATLAS detector using 2011 data*, ATLAS-CONF-2012-020 . https://cds.cern.ch/record/1430034.

[46] ATLAS Collaboration, *Performance of the ATLAS Trigger System in 2010*, Eur.Phys.J. **C72** (2012) 1849.

[47] ATLAS Collaboration, *Jet energy scale and its systematic uncertainty in proton-proton collisions at $\sqrt{s} = 7\,TeV$ with ATLAS 2011 data*, ATLAS-CONF-2013-004 . https://cds.cern.ch/record/1509552.

[48] ATLAS Collaboration, *Single hadron response measurement and calorimeter jet energy scale uncertainty with the ATLAS detector at the LHC*, Eur.Phys.J. **C73** (2013) 2305.

[49] ATLAS Collaboration, *Jet energy measurement and systematic uncertainties using tracks for jets and for b-quark jets produced in proton-proton collisions at $\sqrt{s}=7\,TeV$ in the ATLAS detector*, ATLAS-CONF-2013-002 . https://cds.cern.ch/record/1504739.

[50] ATLAS Collaboration, *Jet energy resolution in proton-proton collisions at $\sqrt{s} = 7\,TeV$ recorded in 2010 with the ATLAS detector*, Eur.Phys.J. **C73** (2013) 2306, arXiv:1210.6210 [hep-ex].

[51] G. Cowan, K. Cranmer, E. Gross, and O. Vitells, *Asymptotic formulae for likelihood-based tests of new physics*, Eur.Phys.J. **C71** (2011) 1554, arXiv:1007.1727 [physics.data-an].

[52] A. L. Read, *Presentation of search results: The CL(s) technique*, J.Phys. **G28** (2002) 2693–2704.

Appendix

A   Triggers

The five triggers used in this analysis are:

- EF_b45_medium_4j45_a4tchad_L2FS: A trigger requiring at least four jets with p_T greater than 45 GeV, at least one of which is b-tagged online. The online b-tagging used has an efficiency to tag b-jets of 50%, evaluated in an MC sample of $t\bar{t}$ events.

- EF_2b35_loose_j145_j35_a4tchad: A trigger requiring at least two online b-tagged jets with p_T greater than 35 GeV, and at least one jet with p_T greater than 145 GeV that may or may not be one of the two b-tagged jets. The online b-tagging used has an efficiency to tag b-jets of 60%, evaluated in an MC sample of $t\bar{t}$ events.

- EF_b45_medium_j145_j45_a4tchad_ht500: A trigger requiring at least one jet with p_T greater than 145 GeV, at least one jet with p_T greater than 45 GeV, one of which is b-tagged online. In addition to this, the trigger also requires the scalar sum of the p_T of all jets in the event with $p_T > 30$ GeV and $|\eta| < 2.5$ to be greater than 500 GeV. The online b-tagging used has an efficiency to tag b-jets of 50%, evaluated in an MC sample of $t\bar{t}$ events.

- EF_j360_a4tchad: A trigger requiring at least one jet with p_T greater than 360 GeV.

- EF_4j80_a4tchad_L2FS: A trigger requiring at least 4 jets with p_T greater than 80 GeV.

The jets used in these triggers are reconstructed using the anti-k_T jet clustering algorithm with radius parameter $R = 0.4$, using topological calorimeter cell clusters as input, and have calibration factors applied that are derived offline. When combined, these triggers give an efficiency of $> 99.5\%$ for $G^* \rightarrow HH \rightarrow b\bar{b}b\bar{b}$ signal MC events passing the full offline selection across the full G^* mass range considered. The individual signal trigger efficiency relative to the offline selection requirements for each trigger is shown in Figure 8. The most important triggers are EF_b45_medium_j145_j45_a4tchad_ht500 and EF_2b35_loose_j145_j35_a4tchad. However, as m_{G^*} increases, the EF_j360_a4tchad trigger helps to recover some of the efficiency lost by these triggers.
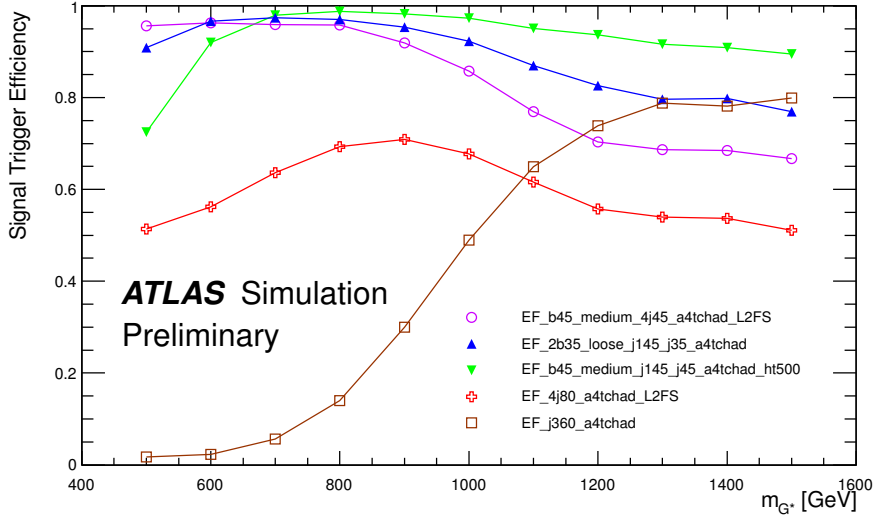
Figure 8: The individual signal trigger efficiency for each of the triggers used in the analysis as a function of the G^* mass. The efficiency shown is relative to the offline analysis selection requirements.

B   Background Prediction

Figure 9 shows the predicted m_{4j} distribution of the multijet and $t\bar{t}$ background contributions in the Signal Region.
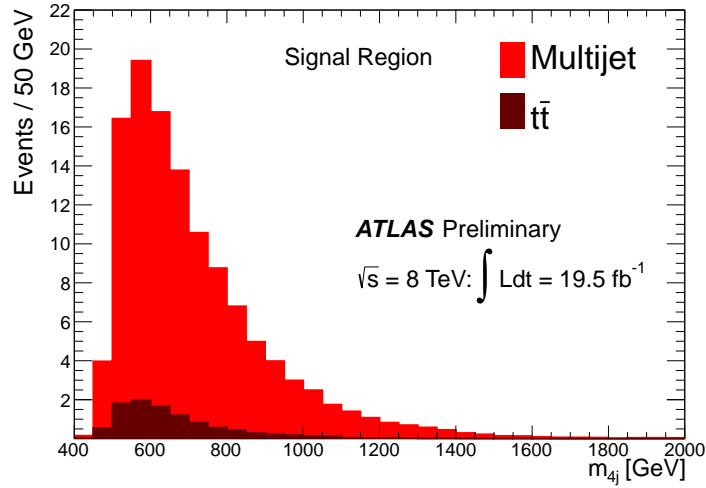

Figure 9: The predicted m_{4j} distribution of the multijet and $t\bar{t}$ background contributions in the Signal Region, shown as stacked histograms. The negligible Z+jets background contribution is not shown.

C Event Display

Figure 10 shows an event display of a candidate $X \rightarrow HH \rightarrow b\bar{b}b\bar{b}$ event in the 2012 data.
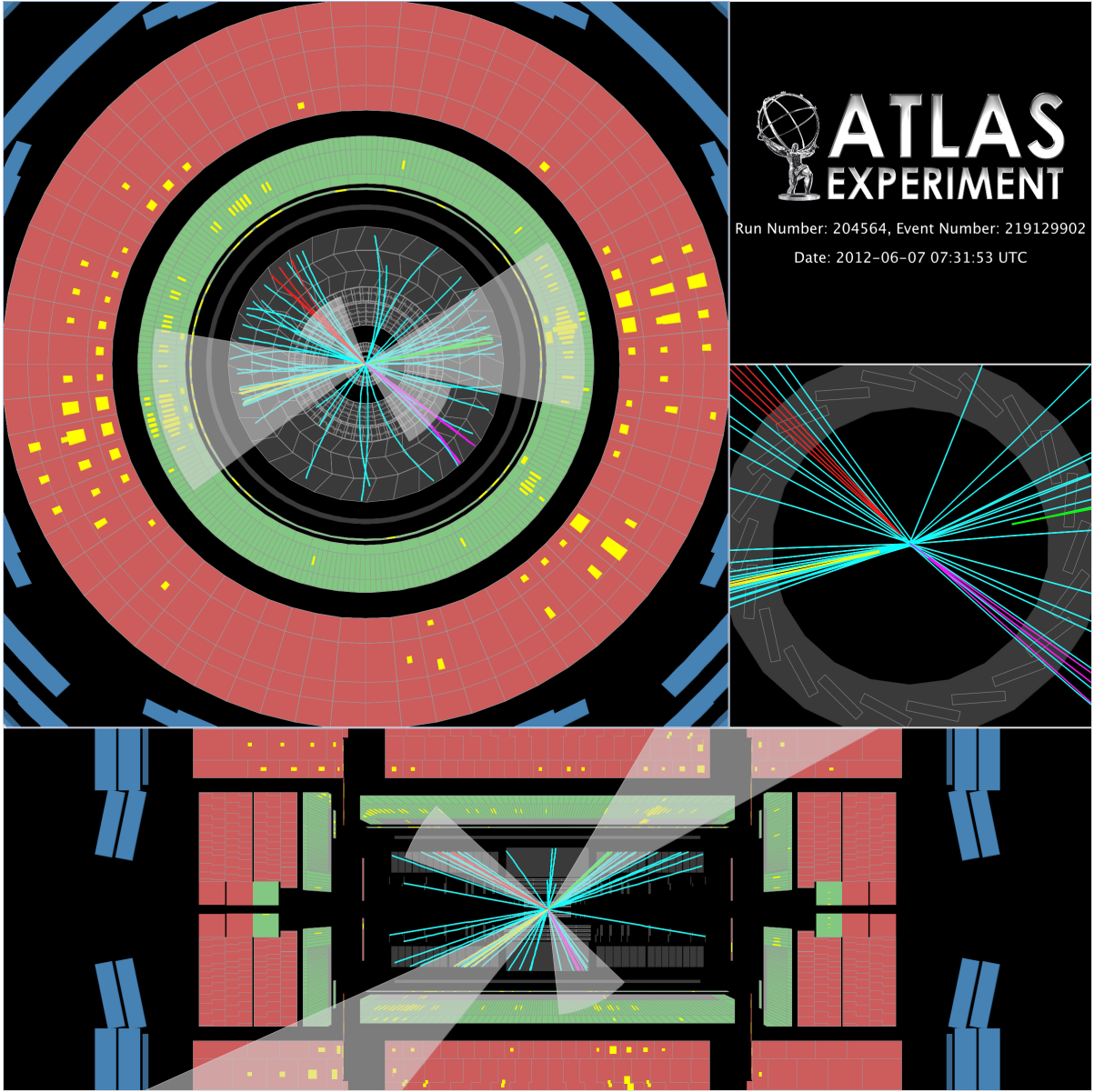

Figure 10: An event display of a candidate $X \rightarrow HH \rightarrow b\bar{b}b\bar{b}$ event in the 2012 data. The two dijets on either side of the event are clearly visible, along with tracks that are associated to an identified secondary vertex (coloured red, yellow, magenta and green). The ($p_{\mathrm{T}}^{\mathrm{dijet}}$, mass, leading jet p_{T}, sub-leading jet p_{T}) of each dijet in this event is $(253, 112, 204, 66)$ GeV and $(230, 115, 193, 61)$ GeV, and $m_{4\mathrm{j}} = 834$ GeV.